Composition Stoichiometry of Cs$_2$AgBiBr$_6$ Films for Highly Efficient Lead-Free Perovskite Solar Cells

Femi Igbari,[†,§] Rui Wang,[‡,§] Zhao-Kui Wang,*[†] Xing-Juan Ma,[†] Qiang Wang,[†] Kai-Li Wang,[†] Yue Zhang,[†] Liang-Sheng Liao,*[†] and Yang Yang*[‡]

[†]Jiangsu Key Laboratory for Carbon-Based Functional Materials & Devices, Institute of Functional Nano & Soft Materials (FUNSOM), Soochow University, Suzhou, Jiangsu 215123, China

[‡]Department of Materials Science and Engineering, University of California, Los Angeles, California 90095, United States

Ⓢ *Supporting Information*

ABSTRACT: Addressing the toxicity issue in lead-based perovskite compounds by seeking other nontoxic candidate elements represents a promising direction to fabricate lead-free perovskite solar cells. Recently, Cs$_2$AgBiBr$_6$ double perovskite achieved by replacing two Pb^{2+} with Ag$^+$ and Bi^{3+} in the crystal lattice has drawn much attention owing to the convenient substitution of its chemical compositions. Herein, the dependence of the optoelectronic properties and corresponding photovoltaic performance of Cs$_2$AgBiBr$_6$ thin films on the deposition methods of vacuum sublimation and solution processing is investigated. Compared to the vacuum sublimation based one, the solution-processed Cs$_2$AgBiBr$_6$ shows inherently higher crystallinity, narrower electronic bandgap, longer photo-excitation lifetime, and higher mobility. The excellent optoelectronic properties are attributed to the accurate composition stoichiometry of Cs$_2$AgBiBr$_6$ films based on solution processing. These merits enable the corresponding perovskite

solar cells to deliver a champion power conversion efficiency (PCE) of 2.51%, which is the highest PCE in the Cs$_2$AgBiBr$_6$-based double perovskite solar cells to date. The finding in this work provides a clear clue that a precise composition stoichiometry could guarantee the formation of high quality multicomponent perovskite films.

KEYWORDS: *Halide double perovskites, Cs$_2$AgBiBr$_6$, solution processing, composition stoichiometry*
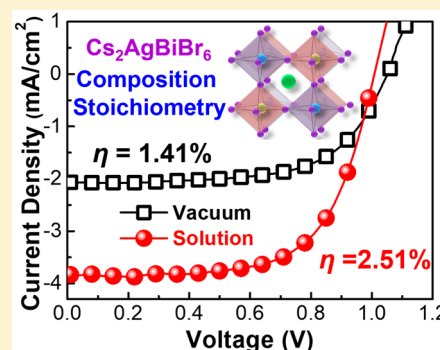
Although the power conversion efficiency (PCE) of lead (Pb) based hybrid organic−inorganic halide perovskite solar cells (PSCs) has exceeded 23%,[1] issues such as stability and the toxicity of Pb have limited the real life consumption of this technology.[2,3] Therefore, it is imperative to address these issues by replacing the Pb content with a nontoxic element and by achieving an all-inorganic compound in which the A-site of the unit cell is occupied by inorganic elements such as Cesium (Cs). Of all the approaches reported to date,[4−13] lead-free halide double perovskites show the best promise of realizing nontoxic and long-term stable PSCs.[8−11] This class of compounds allows the expansion of the perovskite crystal lattice and the substitution of the Pb occupying the B site with two heterovalent cations such as Ag$^+$ and Bi^{3+}.[14−18] The approach yields a double perovskite crystal lattice with a general representation of A$_2$B$^+$B^{3+}X$_6$. However, inferior performance has been reported so far for photovoltaic (PV) devices based on these materials.[19−22] This has been traced to some inherent factors such as electronic band structure which involves a wide bandgap ∼1.98 eV and an indirect bandgap character.[14−16] Beyond such inherent factors, an important external factor that has also contributed to the poor PV performance is the film quality of the halide double perovskite layer.[20,22] Various approaches, such a metal alloying,[17,18] lower dimension (0D, 1D, and 2D) compounds,[23,24] and incorpo-

ration of mixed cations and halides,[25] have been reported to address the aforementioned intrinsic factors. However, the alteration of the intrinsic nature of the compounds is a complicated process. Also, the maintenance of the double perovskite crystal lattice while taking these measures cannot be guaranteed.[26] Therefore, a focus on the external factor by optimizing the thin film deposition techniques could give an insight into advancing the PV performance of halide double perovskite based PSCs.

Vapor deposition and solution processing have been reported in the preparation of halide double perovskite compounds for PV applications. For instance, two-step vapor deposition was used in the preparation of Cs$_2$TiBr$_6$ perovskites.[27] Ke et al. prepared the Cs$_2$SnI$_6$ film via an aerosol assisted chemical vapor deposition technique.[28] Very recently, Wang et al. prepared the Cs$_2$AgBiBr$_6$ films by a sequential vapor deposition technique.[22] Furthermore, solution processing involving low pressure assisted annealing was utilized by Wu et al. for the preparation of Cs$_2$AgBiBr$_6$ films.[19] Because of the merits of easy processability, impressive stability, and
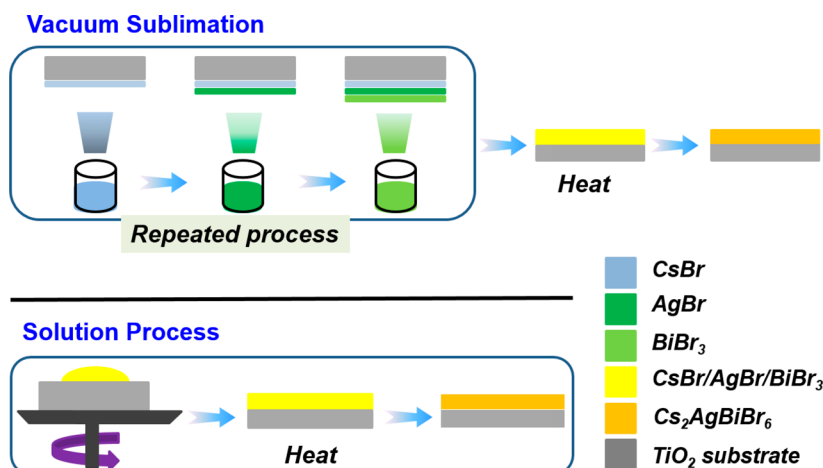
Figure 1. Schematic representation of the preparation of $Cs_2AgBiBr_6$ thin films by vacuum-sublimation and solution-processing.

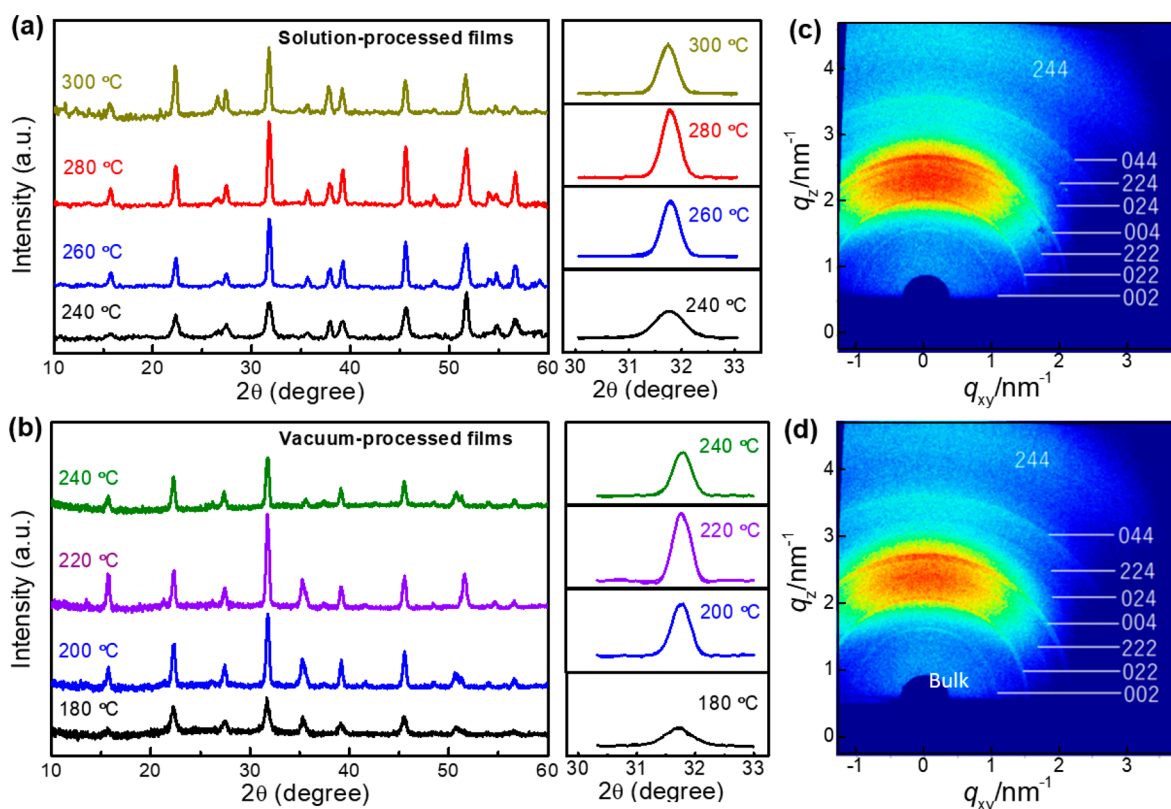**Figure 2.** Annealing temperature dependent XRD patterns and peak fittings of (a)solution- and (b)vacuum-processed $Cs_2AgBiBr_6$ thin films, respectively. 2D GIXRD patterns of (c) solution- and (d) vacuum-processed $Cs_2AgBiBr_6$ thin films annealed at 280 and 220 °C, respectively.

nontoxicity, $Cs_2AgBiBr_6$ stands out as the most studied halide double perovskites. The optoelectronic properties of halide double perovskites are strongly affected by the film deposition methods.[14,16,19,22,29] However, to date, there are no empirical reports on how different preparation methods affect the film quality of these compounds and corresponding device performance. Herein, we compared the pristine $Cs_2AgBiBr_6$ thin films deposited by vacuum sublimation and solution processing with a goal of achieving the precise composition stoichiometry in $Cs_2AgBiBr_6$. The solution-processed $Cs_2AgBiBr_6$ film showed higher crystallinity, narrower electronic bandgap, longer photoexcitation lifetime, and higher mobility than the vacuum-sublimated one. Quantitative X-ray

photoelectron spectra (XPS) analysis revealed the origin of the superior performance of the solution processed films to be a near-stoichiometric existence of its chemical composition. The resulting perovskite solar cells delivered a champion PCE as high as 2.51%. To the best of our knowledge, the PCE presented in this work is the highest efficiency in $Cs_2AgBiBr_6$-based PSCs.

Preparation of Solution- and Vacuum-Processed $Cs_2AgBiBr_6$ Films. The orange crystalline powder of $Cs_2AgBiBr_6$ (Figure S1a) was synthesized by keeping the ratio 2:1:1 of $CsBr/AgBr/BiBr_3$ in HBr with the processes of reflux, evaporation, crystal growth, decanting, and washing. Solution-processed $Cs_2AgBiBr_6$ film was deposited on TiO_2
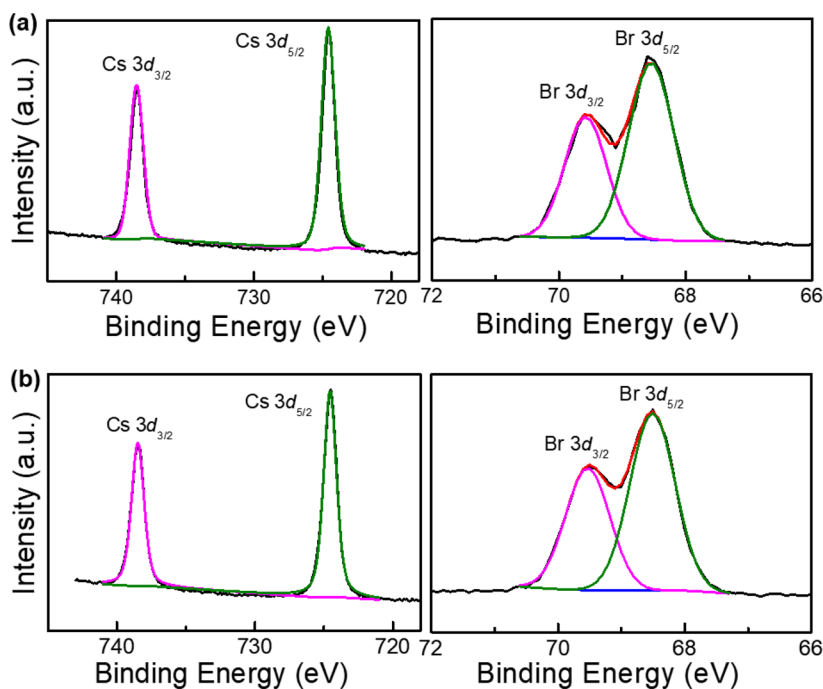
Figure 3. Detailed XPS scans of Cs 3d and Br 3d core levels of (a) solution- and (b) vacuum-processed $Cs_2AgBiBr_6$ thin film.

layer by spin-coating a 0.5 M solution of $Cs_2AgBiBr_6$ in dimethyl sulfoxide (DMSO). Vacuum-sublimated $Cs_2AgBiBr_6$ film was obtained via multiple cycles of sequential deposition of $CsBr$, $AgBr$, and $BiBr_3$ precursor materials at a base pressure of 5.0×10^{-4} Pa (Figure S1d,e,f). Five deposition cycles of $CuBr/AgBr/BiBr_3$ stacks, each with a 2:1:1 molar ratio, were made. Both the vacuum sublimation and solution processing deposition methods yielded $Cs_2AgBiBr_6$ films with a translucent yellow appearance (Figure S1c,g). Subsequent annealing at optimized temperatures of 220 and 280 °C yielded optimized $Cs_2AgBiBr_6$ absorber layers for the vacuum sublimation and solution processing methods, respectively. The thickness of both films was approximately 200 nm. Although there is a discrepancy in the optimized annealing conditions obtained for the vacuum and solution processed films, these conditions fall within the range of those previously reported[20−22,29] for $Cs_2AgBiBr_6$ thin films. We attribute the discrepancy to the difference in the nature of the as-deposited films. The ultrathin nature of the vacuum processed stacked films may have facilitated the thermally induced diffusion reaction required to convert the films into a pure $Cs_2AgBiBr_6$ phase under the given condition. Furthermore, the improved quality observed for the solution processed film at a higher temperature and shorter annealing time can be attributed to the fast removal of the solvent via a high temperature fast solvent evaporation process during annealing. Similar reason has been previously suggested for a mixed-cation perovskite analogue.[30] A schematic diagram showing a comparison of the two different deposition processes is given in Figure 1.

Crystalline Properties of $Cs_2AgBiBr_6$ Films. To understand the morphological properties of the $Cs_2AgBiBr_6$ thin films based on vacuum sublimation and solution processing, their crystallinity and surface morphology were investigated. XRD patterns were obtained for the vacuum-processed films annealed at 180 °C, 200 °C, 220 °C, and 240 °C, and solution-processed films annealed at 240 °C, 260 °C, 280 °C, and 300 °C. The solution-processed films were annealed for 5 min at

the given temperatures to improve the film crystallinity while a more prolonged annealing time of 30 min was required for the vacuum-processed films to allow a nanoscale solid state reaction. XRD results presented in Figure 2a and b showed that the annealed thin films obtained from both deposition processes possessed the same patterns as those previously reported.[22,31,32] There was an increase in peak intensity as the annealing temperature increased in both cases. The highest peak intensities were observed at 220 and 280 °C for the vacuum- and solution-processed film, respectively. To further confirm the optimum annealing temperature, the grain sizes of the crystallites making up the thin films were determined by calculating the crystalline domain sizes. Full-width at half-maximum (fwhm) values, obtained from the Gaussian fit of the most intense peaks of each XRD pattern, were substituted into the Scherrer equation. Details can be found in the Supporting Information (Table S3).

A gradual increase in crystalline domain size was observed from 180 to 220 °C and from 240 to 280 °C, while the domain size decreased at higher temperatures of 240 and 300 °C for the vacuum- and solution-processed film, respectively. Furthermore, higher degree of crystallinity was seen in the solution-processed $Cs_2AgBiBr_6$ film compared to the vacuum-processed one. The realization of $Cs_2AgBiBr_6$ phase with difference in crystallinity was further confirmed by two-dimensional grazing incidence X-ray diffraction (GIXRD), which can evaluate the crystallinity of thin films without interference with the underlyer (Figure 2c,d). The indexed lines agreed well with the $Cs_2AgBiBr_6$ peaks on the XRD patterns (Figure 2a,b). This gradual increase in crystallite size followed by a size decrease and the creation of pinhole defects was further observed from the SEM top images (Figure S2). Full coverage of vacuum- and solution-processed $Cs_2AgBiBr_6$ films was observed up to the optimized annealing temperatures of 220 and 280 °C, respectively. AFM images showing the surface morphologies (Figure S3) further revealed the larger

Table 1. Atomic Ratios of Chemical Composition of Solution- and Vacuum-Processed Cs$_2$AgBiBr$_6$ Thin Films

|	element	core level	binding energy	area	scofield sensitivity	effective area	composition (%)	atom ratio
solution	Cs	$3d_{5/2}$	724.00	23 826.66	23.80	1001.12	20.50	2.01
		$3d_{3/2}$	738.50	19 286.85	16.50	1168.90		
	Ag	$3d_{5/2}$	368.10	5773.72	10.70	539.60	10.30	1.01
		$3d_{3/2}$	374.10	4064.17	7.38	550.70		
	Bi	$4f_{7/2}$	159.18	8314.56	13.90	598.17	10.20	1.00
		$4f_{5/2}$	164.58	5248.90	10.90	481.55		
	Br	$3d_{5/2}$	68.50	5319.54	1.68	3166.39	59.00	5.78
		$3d_{3/2}$	69.50	3571.68	1.16	3079.03		
vacuum	Cs	$3d_{5/2}$	724.60	27 559.92	23.80	1157.98	25.20	2.03
		$3d_{3/2}$	738.50	16 570.62	16.50	1004.28		
	Ag	$3d_{5/2}$	368.10	5989.86	10.70	559.80	12.50	1.01
		$3d_{3/2}$	374.10	3784.17	7.38	512.76		
	Bi	$4f_{7/2}$	159.18	8347.09	13.90	600.51	12.40	1.00
		$4f_{5/2}$	164.58	5051.71	10.90	463.46		
	Br	$3d_{5/2}$	68.50	3757.19	1.68	2236.42	49.90	4.02
		$3d_{3/2}$	69.50	2372.42	1.16	2045.19		
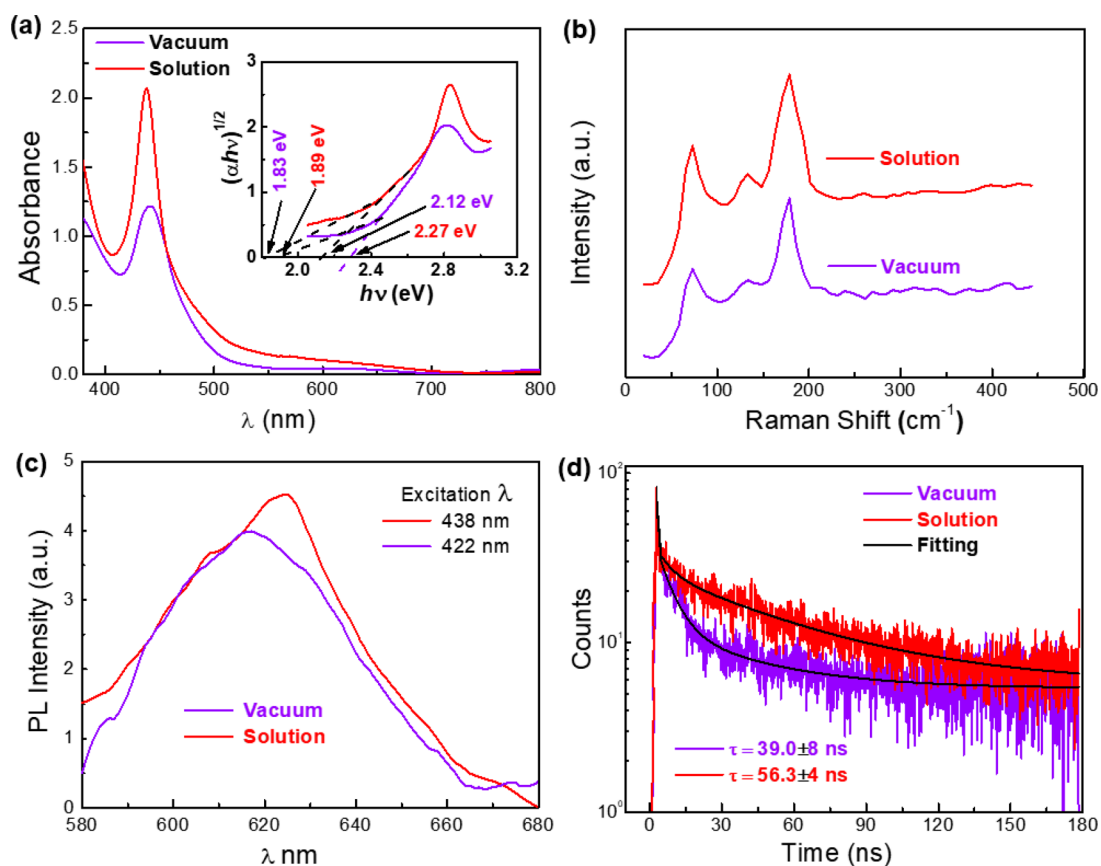
Figure 4. (a) UV−vis absorption spectra, (b) Raman peaks, (c) PL intensity, and (d) PL decay dynamics of the optimized Cs$_2$AgBiBr$_6$ thin films prepared by vacuum-sublimation (purple) and solution-processing (red). Insets of panel a are the Tauc plots extracted from the UV−vis absorption spectra.

crystallite grain size in the solution-processed Cs$_2$AgBiBr$_6$ film than the vacuum-processed one.

Electronic Structure of Cs$_2$AgBiBr$_6$ Films. To investigate the origin of the superior crystalline and morphological properties of the solution-processed Cs$_2$AgBiBr$_6$ film, the actual molar ratios of the elemental compositions in the vacuum- and solution-processed films were determined via postannealing XPS analysis. Figures 3 and S4 present the XPS spectra of Cs 3d, Ag 3d, Bi 4f, and Br 3d core levels in the vacuum-and solution-processed Cs$_2$AgBiBr$_6$ films. The compo-

sition ratios were obtained by processing the data of Cs 3d, Ag 3d, Bi 4f, and Br 3d core levels with XPSPEAK software and Casa XPS program (Casa Software Ltd., UK). The relative sensitivity factors (RSF) provided in the Casa XPS software library were utilized to quantify constituent elements. Table 1 summarizes the detailed parameters for calculating the atomic ratios of the chemical composition of solution- and vacuum-processed Cs$_2$AgBiBr$_6$ thin films. Figure S5 plots the actual atomic component ratios in the vacuum- and solution-processed Cs$_2$AgBiBr$_6$ films. It can be seen that the vacuum-

processed film suffered a larger loss of Br and exhibited a wider deviation from the 2:1:1:6 ratio of Cs/Ag/Bi/Br expected for the $Cs_2AgBiBr_6$ compound. Achieving stoichiometric ratio of Br in the compound's chemical composition is important. This has a significant effect on the quality of the compound formed. According to radius ratio rules, Br^- possesses ionic radius suitable for octahedral coordination with Ag^+ in the double perovskite crystal lattice.[14] This ensures the formation of a stable compound. Furthermore, halogens can modulate the bandgap of the perovskite compound. The bandgap of halide double perovskites decreases with increasing ionic radius of the halide at the X site (i.e., F^-, Cl^-, Br^-, I^-).[33] Interestingly, Br^- yields the most stable Cs_2AgBiX_6 compound[26] with a bandgap most suitable for PV applications.[19,20] In addition, bromine deficiency may result in the formation of point defects such as bromine vacancies (V_{Br}) in the compound.[34] These point defects are stable because they require low formation energies. They are identified as deep electron traps. The defects also affect the electronic band structure and may partly account for inferior photophysical properties in a bromine deficient compound. Although partial Br may have been lost in our vacuum-processed film as gaseous bromine during annealing, the larger loss of gaseous Br may have resulted from the transformation of the precursor material into vapor form during vacuum deposition. Annealing the vacuum-processed $Cs_2AgBiBr_6$ films in a Br vapor atmosphere may mitigate this loss. However, an in-depth understanding of the modulation of Br ratio is required to achieve high-quality $Cs_2AgBiBr_6$ films with reduced low-energy-forming deep level defects. This stems from the conflicting reports on the best crystal growth conditions for this compound. For instance, Xiao et al.[26] predicted a Br-poor/Bi-rich condition, while Li et al.[34] reported a Br-rich/Bi-poor condition. Furthermore, the XRD patterns of vacuum- and solution-processed $Cs_2AgBiBr_6$ films were investigated by heating them at 100 °C in ambient for 300 h. Although there was a slight reduction in the intensities for both films, no appearance of new crystal phase and no changes of the XRD peak patterns were observed after a long time and high temperature aging (Figure S6).

Photophysical Properties of $Cs_2AgBiBr_6$ Films. For the thin films to be suitable for PV application, it is important to understand the photophysical properties of $Cs_2AgBiBr_6$ films. Therefore, UV−vis absorption, steady state photoluminescent (PL) spectra, and time-resolved PL (TRPL) spectra of $Cs_2AgBiBr_6$ films were conducted to study their photophysical properties. Figure 4a shows the UV−vis absorption spectra for both samples. Insets are the Tauc plots extracted from the UV−vis absorption spectra. A sharp peak could be seen at 438 and 442 nm on the absorption spectra of the solution- and vacuum-processed $Cs_2AgBiBr_6$ films, respectively. Since there is no monotonic variation between crystallite size and peak shape, the existence of such peaks did not result from quantum confined excitonic transitions. Therefore, the peaks are ascribed to $s-p$ transitions occurring in bismuth (Bi). Furthermore, the Tauc plots confirmed the indirect bandgap character in the two films. Values of phonon assisted transition energies of 1.83 and 2.12 eV were obtained for the solution-processed film, which indicated a bandgap of 1.98 eV, whereas the vacuum-processed film presented phonon assisted energies of 1.89 and 2.27 eV, which gave a bandgap of 2.08 eV. These results mean that the transitions in the solution- and vacuum-processed $Cs_2AgBiBr_6$ films were assisted by phonon energies of 0.29 and 0.38 eV, respectively. Although the two films were

made of the same compound, the bandgaps extracted from their Tauc plots had different values. This stemmed from the difference in the pattern of their absorption spectra. Higher absorbance could be seen in the solution-processed film compared with the vacuum-processed one. Such difference in pattern affected the corresponding Tauc plot parameters. Therefore, the difference in bandgap values was associated with the difference in film deposition method. Factors such as the differences in preparation method,[15,33] characterization techniques,[14,15,35] structural models,[36,37] and disorder in atomic arrangements[38] have been previously reported to be responsible for the wide range of bandgap values of $Cs_2AgBiBr_6$. Figure 4b shows the Raman spectroscopies of two samples. The similarity in Raman peak positions indicates that both films possess the same elemental components.[39,40] However, the observed difference in peak intensities reveal a gradation in degree of crystallinity in the films.[41−43] The variation in peak intensity can be ascribed to the variation in phonon energies in the crystal lattice. There exists a monotonic relationship between degree of crystallinity, phonon energy, and peak intensity.[42]

The PL spectra of the solution- and vacuum-processed $Cs_2AgBiBr_6$ films are presented in Figure 4c. Bandgap values of 2.01 and 1.99 eV were obtained from the probe wavelengths of 616 and 624 nm for the vacuum- and solution-processed $Cs_2AgBiBr_6$ films, respectively. The values are within the range of those obtained from the Tauc plots. The PL decay kinetics of the two films are shown in Figure 4d. The curves can be separated into initial rapid decay followed by an intermediate decay and a prolonged decay. Therefore, corresponding three different lifetime components, τ_1, τ_2, and τ_3, can be assigned to the photoexcited charges in the thin films. For the solution processed film, the values obtained for τ_1, τ_2, and τ_3 were 0.16 ± 0.02 ns (8%), 5.8 ± 1.14 ns (29%), and 56.3 ± 4.0 ns (63%), respectively, whereas the vacuum-processed film yielded 0.16 ± 0.01 ns (9%), 6.7 ± 0.5 ns (33%), and 39.0 ± 8 ns (58%), respectively. The lifetimes of the rapid PL decay components of the solution- and vacuum-processed films are comparable. The same is also seen for the intermediate decay components of both films. However, their prolonged PL decay components exhibited a wide difference in lifetime. The rapid and intermediate decay components likely resulted from the defects such as surface traps or recombination involving less mobile excitons. However, the long PL decay component was ascribed to the intrinsic charge carrier recombination. As a result, the long PL decay component would give the fundamental recombination lifetime of the films.[14] Therefore, using Fick's first law of diffusion (eq 1), the room temperature diffusion coefficients (D) for both films were estimated from their prolonged PL decay components:

$$J = -D\frac{dc}{dx} \qquad (1)$$

where J is the diffusion flux, D is the diffusion coefficient, and dc/dx is the charge carrier concentration gradient. Subsequent calculations using D yielded mobility values of 0.39 $cm^2/(V\ s)$ and 0.74 $cm^2/(V\ s)$ for the vacuum- and solution-processed films, respectively. Compared to the vacuum-processed film, the solution-processed film exhibits higher mobility. Moreover, the extracted mobility values are far lower than those exhibited by the standard $MAPbI_3$ perovskites.[44,45] This, among other factors, is responsible for the low-performance commonly reported for $Cs_2AgBiBr_6$-based solar cells.

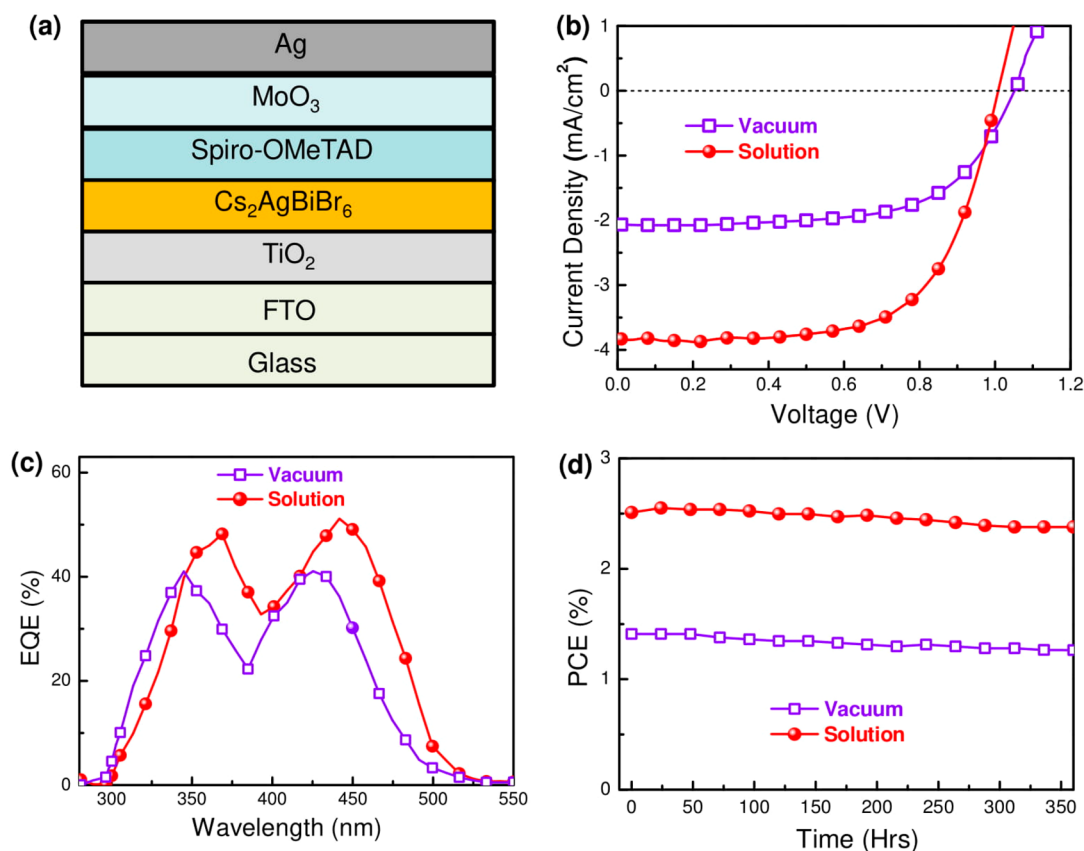**Figure 5.** (a) Device structure: FTO/TiO$_2$/Cs$_2$AgBiBr$_6$/Spiro-OMeTAD/MoO$_3$/Ag. (b) J–V curves, (c) EQE spectra, and (d) ambient stability characteristics of the perovskite solar cells fabricated with optimized solution- and vacuum-processed Cs$_2$AgBiBr$_6$ thin films.

Table 2. Cell Parameters of Cs$_2$AgBiBr$_6$-based PSCs Using Different Deposition Methods

	deposition method	J_{sc} (mA/cm^2)	V_{oc} (V)	FF	PCE (%)
champion	solution	3.82	1.01	0.65	2.51
	vacuum	2.06	1.05	0.65	1.41
average	solution	3.81 ± 0.01	1.00 ± 0.03	0.63 ± 0.02	2.48 ± 0.03
	vacuum	2.05 ± 0.02	1.03 ± 0.02	0.62 ± 0.03	1.35 ± 0.06

Photovoltaic Performance. The planar perovskite solar cells with an n−i−p structure of FTO/TiO$_2$/perovskite/Spiro-OMeTAD/MoO$_3$/Ag (Figure 5a) were fabricated to investigate the photovoltaic performance of solution- and vacuum-processed Cs$_2$AgBiBr$_6$ films. The annealing temperature was optimized to be 220 and 280 °C for vacuum- and solution-processed devices, respectively (Figure S7, Table S4). As shown in Figure 5b, the champion solution- and vacuum-processed devices presented PCEs of 2.51% and 1.41%, respectively. The 80 devices fabricated, in each case, confirmed the reproducibility of efficiency (Figure S8), producing the average PCEs of 2.48 ± 0.03% and 1.35 ± 0.06% for solution- and vacuum-processed devices, respectively. As shown in Table 2, the obtained photovoltaic parameters for the champion devices are far inferior to those already possessed by the lead-based perovskites. This can be attributed to the less suitable electronic and photophysical properties of a Cs$_2$AgBiBr$_6$ thin film, which commonly possess a wide bandgap ≥ 1.95 eV with indirect character and low charge carrier mobility.[14] Interestingly, there was a 78% increase in the PCE when the vacuum sublimation method was replaced with solution processing technique to deposit the Cs$_2$AgBiBr$_6$ film. As aforementioned, owing to the almost accurate composition stoichiometry of

Cs$_2$AgBiBr$_6$, the solution-processed Cs$_2$AgBiBr$_6$ film exhibited excellent optoelectronic and photophysical properties with higher crystallinity, narrower electronic bandgap, longer photoexcitation lifetime, and higher mobility. These merits enable the corresponding perovskite solar cells to deliver a champion power conversion efficiency (PCE) of 2.51%. Furthermore, the champion solution-processed device exhibited negligible hysteresis (Figure S9a). The reverse scan showed J_{sc} = 3.82 mA/cm^2, V_{oc} = 1.01 V, FF = 0.65, and PCE = 2.51% as presented in Table 2. The forward scan had J_{sc} = 3.82 mA/cm^2, V_{oc} = 1.01 V, FF = 0.64, and PCE = 2.47%. On the contrary, the champion vacuum-processed device exhibited significant hysteresis (Figure S9b) with the reverse scan having J_{sc} = 2.06 mA/cm^2, V_{oc} = 1.05 V, FF = 0.65, and PCE = 1.41%, while the forward scan yielded J_{sc} = 2.05 mA/cm^2, V_{oc} = 1.04 V, FF = 0.57, and PCE = 1.22%. The observed difference in the hysteretic response of the two devices can be attributed to the morphological and photophysical differences in their properties as a result of difference in stoichiometry. The solution processed device structure exhibited a more efficient interfacial charge extraction between Cs$_2$AgBiBr$_6$ and the charge transport layers. This may be due to a suppressed

heterojunction charge accumulation resulting from a reduced trapping/detrapping of photogenerated charge carriers.[46]

Furthermore, the external quantum efficiency (EQE) values of both devices are presented in Figure 5c. The EQE is the ratio of the amount of current created by the solar cell to the amount of photons of a given energy from the incident photons. It can be seen that the higher current was generated in the solution-processed device for the same photon energy. The overall generation of current by high energy photons (with shorter wavelength ≤550 nm) was ascribed to the wide and indirect bandgap character of the absorber layers. Figure 5d shows the results for the stability tests of vacuum- and solution-processed PSCs. The devices were kept in ambient without encapsulation for 15 days. Both devices were able to retain over 90% of their initial PCEs. The ambient stability obtained for the two devices are greater than those of standard MAPbI$_3$ based devices and can be traced to the stability of the Cs$_2$AgBiBr$_6$ absorber layers.

Conclusion. In summary, a comparison has been executed by preparing Cs$_2$AgBiBr$_6$ halide double perovskite via vacuum-sublimation and solution-processing. The solution-processed film exhibited higher crystallinity, lower bandgap, longer charge carrier lifetime, and higher mobility compared to the vacuum-processed one. Optimized power conversion efficiencies of 2.51% and 1.41% were obtained for the solution- and vacuum-processed films, respectively, as a result of the differences in their optoelectronic and photophysical properties. Although immense research is still required to improve the performance of halide double perovskite based devices, the finding in this work gives a hint that a wide deviation from ideal stoichiometry is responsible for lower film quality and device performance, whereas solution-processing film deposition technique could guarantee a precise composition stoichiometry to form high quality multicomponent perovskite films.

ASSOCIATED CONTENT

Ⓢ Supporting Information

The Supporting Information is available free of charge on the ACS Publications website at DOI: 10.1021/acs.nanolett.9b00238.

Experimental section, supporting figures, tables, and equations (PDF)

AUTHOR INFORMATION

Corresponding Authors

*E-mail: zkwang@suda.edu.cn.
*E-mail: lsliao@suda.edu.cn.
*E-mail: yangy@ucla.edu.

ORCID Ⓞ

Zhao-Kui Wang: 0000-0003-1707-499X
Liang-Sheng Liao: 0000-0002-2352-9666
Yang Yang: 0000-0001-8833-7641

Author Contributions

§F.I. and R.W. contributed equally to this work.

Notes

The authors declare no competing financial interest.

ACKNOWLEDGMENTS

REFERENCES

(1) Zhao, D.; Wang, C.; Song, Z.; Yu, Y.; Chen, C.; Zhao, X.; Zhu, K.; Yan, Y. 23%. *ACS Energy Lett.* **2018**, *3*, 305−206.

(2) Babayigit, A.; Ethirajan, A.; Muller, M.; Conings, B. *Nat. Mater.* **2016**, *15*, 247−251.

(3) Liu, F.; Dong, Q.; Wong, M. K.; Djurisic, A. B.; Ng, A.; Ren, Z.; Shen, Q.; Surya, C.; Chan, W. K.; Wang, J.; Ng, A. M. C.; Liao, C.; Li, H.; Shih, K.; Wei, C.; Su, H.; Dai, J. *Adv. Energy Mater.* **2016**, *6*, 1502206.

(4) Gao, W.; Ran, C.; Li, J.; Dong, H.; Jiao, B.; Zhang, L.; Lan, X.; Hou, X.; Wu, Z. *J. Phys. Chem. Lett.* **2018**, *9*, 6999−7006.

(5) Konstantakou, M.; Stergiopoulos, T. *J. Mater. Chem. A* **2017**, *5*, 11518−11549.

(6) Krishnamoorthy, T.; Ding, H.; Yan, C.; Leong, W. L.; Baikie, T.; Zhang, Z. Y.; Sherburne, M.; Li, S.; Asta, M.; Mathews, N.; Mhaisalkar, S. G. *J. Mater. Chem. A* **2015**, *3*, 23829−23832.

(7) Shi, Z. J.; Guo, J.; Chen, Y. H.; Li, Q.; Pan, Y. F.; Zhang, H. J.; Xia, Y. D.; Huang, W. *Adv. Mater.* **2017**, *29*, 1605005.

(8) Heo, J. H.; Kim, J.; Kim, H.; Moon, S. H.; Im, S. H.; Hong, K.-H. J. *J. Phys. Chem. Lett.* **2018**, *9*, 6024−6031.

(9) Stoumpos, C. C.; Frazer, L.; Clark, D. J.; Kim, Y. S.; Rhim, S. H.; Freeman, A. J.; Ketterson, J. B.; Jang, J. I.; Kanatzidis, M. G. *J. Am. Chem. Soc.* **2015**, *137*, 6804−6819.

(10) Zhang, Q.; Hao, F.; Li, J.; Zhou, Y.; Wei, Y.; Lin, H. *Sci. Technol. Adv. Mater.* **2018**, *19*, 425−442.

(11) Marshall, K. P.; Walker, M.; Walton, R. I.; Hatton, R. A. *Nat. Energy* **2016**, *1*, 1.

(12) Jain, S. M.; Phuyal, D.; Davies, M. L.; Li, M.; Philippe, B.; De Castro, C.; Qiu, Z.; Kim, J.; Watson, T.; Tsoi, W. C.; Karis, O.; Rensmo, H.; Boschloo, G.; Edvinsson, T.; Durrant, J. R. *Nano Energy* **2018**, *49*, 614−624.

(13) Kim, Y.; Yang, Z.; Jain, A.; Voznyy, O.; Kim, G.-H.; Liu, M.; Quan, L. N.; Garcia de Arquer, F. P.; Comin, R.; Fan, J. Z.; Sargent, E. H. *Angew. Chem., Int. Ed.* **2016**, *55*, 9586−9590.

(14) Slavney, A. H.; Hu, T.; Lindenberg, A. M.; Karunadasa, H. I. *J. Am. Chem. Soc.* **2016**, *138*, 2138−2141.

(15) McClure, E. T.; Ball, M. R.; Windl, W.; Woodward, P. M. *Chem. Mater.* **2016**, *28*, 1348−1354.

(16) Volonakis, G.; Filip, M. R.; Haghighirad, A. A.; Sakai, N.; Wenger, B.; Snaith, H. J.; Giustino, F. *J. Phys. Chem. Lett.* **2016**, *7*, 1254−1259.

(17) Du, K.-Z.; Meng, W.; Wang, X.; Yan, Y.; Mitzi, D. B. *Angew. Chem., Int. Ed.* **2017**, *56*, 8158−8162.

(18) Du, K.-Z.; Wang, X.; Han, Q.; Yan, Y.; Mitzi, D. B. *ACS Energy Lett.* **2017**, *2*, 2486−2490.

(19) Wu, C.; Zhang, Q.; Liu, Y.; Luo, W.; Guo, X.; Huang, Z.; Ting, H.; Sun, W.; Zhong, X.; Wei, S.; Wang, S.; Chen, Z.; Xiao, L. *Adv. Sci.* **2018**, *5*, 1700759.

(20) Ning, W.; Wang, F.; Wu, B.; Lu, J.; Yan, Z.; Liu, X.; Tao, Y.; Liu, J.-M.; Huang, W.; Fahlman, M.; Hultman, L.; Sum, T. C.; Gao, F. *Adv. Mater.* **2018**, *30*, 1706246.

(21) Greul, E.; Petrus, M. L.; Binek, A.; Docampo, P.; Bein, T. *J. Mater. Chem. A* **2017**, *5*, 19972−19981.

(22) Wang, M.; Zeng, P.; Bai, S.; Gu, J.; Li, F.; Yang, Z.; Liu, M. *Sol. RRL* **2018**, *2*, 1800217.

(23) Connor, B. A.; Leppert, L.; Smith, M. D.; Neaton, J. B.; Karunadasa, H. I. *J. Am. Chem. Soc.* **2018**, *140*, 5235−5240.

(24) Tang, G.; Xiao, Z.; Hosono, H.; Kamiya, T.; Fang, D.; Hong, J. *J. Phys. Chem. Lett.* **2018**, *9*, 43−48.

(25) Volonakis, G.; Haghighirad, A. A.; Snaith, H. J.; Giustino, F. *J. Phys. Chem. Lett.* **2017**, *8*, 3917−3924.

(26) Xiao, Z.; Meng, W.; Wang, J.; Yan, Y. *ChemSusChem* **2016**, *9*, 2628−2633.

(27) Chen, M.; Ju, M.-G.; Carl, A. D.; Zong, Y.; Grimm, R. L.; Gu, J.; Zeng, X. C.; Zhou, Y.; Padture, N. P. *Joule* **2018**, *2*, 558−570.

(28) Ke, J. C.-R.; Lewis, D. J.; Walton, A. S.; Spencer, B. F.; O'Brien, P.; Thomas, A. G.; Flavell, W. R. *J. Mater. Chem. A* **2018**, *6*, 11205−11214.

(29) Gao, W.; Ran, C.; Xi, J.; Jiao, B.; Zhang, W.; Wu, M.; Hou, X.; Wu, Z. *ChemPhysChem* **2018**, *19*, 1696−1700.

(30) Kim, M.; Kim, G.-H.; Oh, K. S.; Jo, Y.; Yoon, H.; Kim, K.-H.; Lee, H.; Kim, J. Y.; Kim, D. S. *ACS Nano* **2017**, *11*, 6057−6064.

(31) Yang, B.; Chen, J.; Yang, S.; Hong, F.; Sun, L.; Han, P.; Pullerits, T.; Deng, W.; Han, K. *Angew. Chem., Int. Ed.* **2018**, *57*, 5359−5363.

(32) Zhou, L.; Xu, Y.-F.; Chen, B.-X.; Kuang, D.-B.; Su, C.-Y. *Small* **2018**, *14*, 1703762.

(33) Filip, M. R.; Hillman, S.; Haghighirad, A.-A.; Snaith, H. J.; Giustino, F. *J. Phys. Chem. Lett.* **2016**, *7*, 2579−2585.

(34) Li, T.; Zhao, X.; Yang, D.; Du, M.-H.; Zhang, L. *Phys. Rev. Appl.* **2018**, *10*, 041001.

(35) Bartesaghi, D.; Slavney, A. H.; Gelvez-Rueda, M. C.; Connor, B. A.; Grozema, F. C.; Karunadasa, H. I.; Savenije, T. J. *J. Phys. Chem. C* **2018**, *122*, 4809−4816.

(36) Savory, C. N.; Walsh, A.; Scanlon, D. O. *ACS Energy Lett.* **2016**, *1*, 949−955.

(37) Han, D.; Zhang, T.; Huang, M.; Sun, D.; Du, M.-H.; Chen, S. *APL Mater.* **2018**, *6*, 084902.

(38) Zhao, X.; Yang, J.; Fu, Y.; Yang, D.; Xu, Q.; Yu, L.; Wei, S.-H.; Zhang, L. *J. Am. Chem. Soc.* **2017**, *139*, 2630−2638.

(39) Ha, S. T.; Liu, X.; Zhang, Q.; Giovanni, D.; Sum, T. C.; Xiong, Q. *Adv. Opt. Mater.* **2014**, *2*, 838−844.

(40) Xie, L.-Q.; Zhang, T.-Y.; Chen, L.; Guo, N.; Wang, Y.; Liu, G.-K.; Wang, J.-R.; Zhou, J.-Z.; Yan, J.-W.; Zhao, Y.-X.; Mao, B.-W.; Tian, Z.-Q. *Phys. Chem. Chem. Phys.* **2016**, *18*, 18112−18118.

(41) Edinger, M.; Knopp, M. M.; Kerdoncuff, H.; Rantanen, J.; Rades, T.; Löbmann, K. *Eur. J. Pharm. Sci.* **2018**, *117*, 62−67.

(42) Joya, M. R.; Fonseca, K. M.; Barba-Ortega, J. *AIP Conf. Proc.* **2014**, *1627*, 42−45.

(43) Quarti, C.; Grancini, G.; Mosconi, E.; Bruno, P.; Ball, J. M.; Lee, M. M.; Snaith, H. J.; Petrozza, A.; De Angelis, F. *J. Phys. Chem. Lett.* **2014**, *5*, 279−284.

(44) Hutter, E. M.; Eperon, G. E.; Stranks, S. D.; Savenije, T. J. *J. Phys. Chem. Lett.* **2015**, *6*, 3082−3090.

(45) Guo, Z.; Manser, J. S.; Wan, Y.; Kamat, P. V.; Huang, L. *Nat. Commun.* **2015**, *6*, 7471.

(46) Snaith, H. J.; Abate, A.; Ball, J. M.; Eperon, G. E.; Leijtens, T.; Noel, N. K.; Stranks, S. D.; Wang, J. T. W.; Wojciechowski, K.; Zhang, W. *J. Phys. Chem. Lett.* **2014**, *5*, 1511−1515.